

Ground-Glass Nodule Characterization in High-Resolution CT Scans

Kazunori Okada

Computer Science Department

San Francisco State University

kazokada@sfsu.edu

Abstract

This chapter presents a comprehensive review of the literature related to ground-glass nodules (GGNs) and evaluates effectiveness of RAGF algorithm, proposed by our previous work [45, 46], for pulmonary nodule characterization of GGN cases in the high-resolution computed tomography (HRCT) images. The literature on GGNs in radiology, pathology and medical image analysis are surveyed and discussed. The nomenclature for GGNs are also summarized in order to clarify some confusion in the literature. The RAGF algorithm is evaluated by using a HRCT dataset consisting of 56 GGN cases. This chapter outlines the RAGF algorithm in some detail and discusses the experimental results with the GGN dataset.

Keywords: Ground-glass nodules; part- and non-solid nodules; X-ray computed tomography; pulmonary nodules; nodule segmentation; nodule volumetry

1 Introduction: Literature Review

Lung cancer is the most common cause of cancer death in the U.S. for both sexes [61]. Among various types of the small-cell and non-small-cell lung cancers, adenocarcinoma is the most preva-

lent type, accounting for more than a third of all primary lung tumors, and its incidence has been increasing in past a few decades. [14]. X-ray computed tomography (CT) is the most sensitive imaging domain for non-invasive diagnostics of adenocarcinomas among others [26]. The recent advances in 3D imaging technology, such as high-resolution and multi-detector CT, has greatly improved image resolution and scanning time [6], making it possible to detect very small lung tumors. Study of such small tumors is clinically important because they can still be malignant and early detection of such malignancy can increase the chance of patient survival [44]. This technical advent has also helped us to better understand the intricate pathology of a type of adenocarcinoma known as *small peripheral adenocarcinomas* [42]. *Ground-glass nodule (GGN)* is the common radiographic appearance of such small peripheral lung adenocarcinomas [14].

1.1 Radiographic Characteristics of GGNs

Radiologically speaking, GGN represents a type of pulmonary nodules (i.e., localized increase of attenuation in the lung parenchyma of a X-ray CT image), which does not completely obscure the underlying normal parenchymal structures such as airways, vessels and interlobular septa (i.e., presenting a focal ground-glass opacity or *GGO*). GGN is also known as *subsolid* nodule, while those that completely obscure the lung parenchyma are called *solid* nodules. GGN covers a spectrum between completely-not-solid and almost-solid opacities, which are clinically categorized into two subtypes: *pure* and *mixed* GGNs. For the pure GGNs, the appearance of the entire nodule is subsolid, while the mixed GGNs consists of a combination of solid and subsolid components.

1.2 Nomenclature of GGNs

There exist varying, sometimes confusing, terms denoting these radiographic classifications. In literature, GGNs has equivalently been called as GGOs [32], focal GGOs [41], localized GGOs [40], nodular GGOs [47], localized/focal GGAs (ground-glass attenuation) [12], subsolid nodules [14], nonsolid nodules [9], or semisolid nodules [27]. The pure GGNs are also called *nonsolid* nodules [19], while the mixed GGNs are called *part-solid* nodules [19] or *heterogeneous* GGOs [63].

1.3 Clinical Prevalence: Epidemiology

GGNs are clinically significant because they are the CT appearance of a prevalent and highly malignant class of lung cancers, offering an effective and non-invasive screening and diagnostic means. The spectrum of the small peripheral adenocarcinomas represented by GGNs has been histologically classified by Noguchi [42] and WHO [59], including special types of the pre-malignant atypical adenomatous hyperplasia (AAH), the malignant bronchioloalveolar carcinoma (BAC), and more invasive mixed subtype adenocarcinoma. BAC corresponds to Noguchi's type A, B and C classifications and is the most common form of adenocarcinoma, accounting for 74% of all adenocarcinomas and 2-6% of all non-small-cell lung cancers. When combining the BAC with the incidence of the mixed subtype adenocarcinoma with a BAC component, the combined class accounts for 20% of all lung cancers [14].

1.4 Malignancy of GGNs

The radiographic findings of the pure and mixed GGNs have been shown to correspond roughly to the AAH, BAC and other adenocarcinomas [12, 32, 63, 40, 54, 24]. GGNs are most likely malignant [9]. And the mixed GGNs are shown to have much higher chance of malignancy than pure GGNs and solid nodules. In a screening study by Henschke et al. [19], the mixed GGNs recorded a malignancy rate of 63% while the pure GGNs and solid nodules were malignant only in 8% and 7% cases, respectively. Several studies have also shown that greater GGO components in the mixed GGN cases correlate with lesser chance of malignancy [41, 35, 47] and better prognosis [2, 24, 33]. Despite these findings, the value of CT for differentiating benign and malignant GGNs has not been confirmed because there are reports with mixed results in literature [14].

1.5 GGNs' Evolution and Histopathological Disease Progression

Studying the subtypes of GGNs are also important for understanding the histopathological evolution of the peripheral adenocarcinomas. The pure GGNs that are less than 5mm in size nearly

always corresponds to AAH, while the larger pure and mixed GGNs should be treated malignant as BAC or invasive adenocarcinoma [41, 14]. It has been observed that at least some cases of benign AAH slowly progress to malignant BAC and to more invasive adenocarcinoma [21, 1, 56, 22] thus early detection and treatment of pure GGO can also improve a prognosis of lung cancer [60]. The growth pattern of these GGNs are however confusing. Many cases do not show increase in nodule size, and in some cases the nodule size can even decrease over time while being malignant [39]. In general, the evolution from AAH to malignant adenocarcinoma is very slow [39] and may not be hypermetabolic at FDG-PET [9] thus requiring a longer interval in a CT follow-up study with more accurate volumetry/change-estimation scheme. This poses a difficult technical challenge since the subsolid opacity of GGNs makes accurate and repeatable 3D lesion segmentation a challenging task, and such accurate segmentation is a prerequisite for an accurate volumetry/change-estimation [64, 29, 48, 20, 13].

1.6 Computer-Aided Detection and Diagnosis of GGNs

Computer-aided detection (CADe) and diagnosis (CADx) for pulmonary nodules is a well-studied field. The improved 3D image resolution helps radiologists detect nodules more accurately [11], however it also creates more of a burden increasing the amount of data they need to interpret. Thus, automation of the analysis with computer-assisted systems is much needed for reducing this burden and also improving the diagnostic accuracy especially for the small nodules. Despite the vast existing literature on general lung CAD [49, 26, 50, 37, 52, 36, 15], studies on applying the CAD approach to GGNs still under-represent the above clinical interests in the literature. Three different steps, detection [10, 57, 25, 4, 70, 23, 65, 58], segmentation [67, 46, 68, 70, 66, 5, 31, 53, 58], and classification [55, 43, 69], of the GGN CAD scheme have been studied by a number of investigators. For GGN detection, most approaches exploit either image processing filters (N-Quoit filter [10, 57] and Gabor filter [4]) or machine learning-based classifiers (three-layer ANN [25] and LDA [23, 58]). Only a few previous studies exist for classification of GGN subtypes. Suzuki et al. [55] proposed a CAD scheme for classifying malignancy of pulmonary nodules by using the massive training artificial neural network. Odry et al. [43] proposed an algorithm to automatically

estimate the amount of solid components in GGNs. Zheng et al. [69] introduced a voxel-wise ground-glass opacity index feature that can be used for other applications. For segmentation, various proposals have been made in the literature. The proposed algorithms include robust anisotropic Gaussian fitting [46], shape-based Markov random field [67, 68], non-parametric 3D texture likelihood map analysis [70], 4-phase level set segmentation [66], 6-stage region growing [31], and LDA-based machine learning approach [5, 58]. Most studies focus on maximizing segmentation accuracy rather than robustness/reproducibility. Despite these increasing interests, GGN-CAD remains an open problem with much room for improvement especially in robustness.

1.7 Lung Nodule Volumetry and Its Limitation

Toward realizing a robust volumetry/change-estimation of GGNs in order to diagnose small AAH and BAC more reliably and uncover more details of the peripheral adenocarcinomas' disease progression, this study focuses on the segmentation part of the overall GGN-CAD. Segmentation applied in volumetry (i.e., estimation of volume change over time or measuring the doubling time) brings more emphasis to its robustness/reproducibility than its raw accuracy as a domain-specific criterion. Recent studies on CT nodule volumetry have revealed considerable variability in the existing software's estimation results when varying CT reconstruction parameters [17], CT dosage setting [18], software versions [51], algorithm choice [3] and algorithm threshold parameters [17]. These inaccuracies limit the time-interval of follow-up studies to be some large values, reducing its clinical usability [30]. Note that a fixed-value bias in segmentation error is canceled out when measuring volumetry so that even an inaccurate segmentation algorithm can be a good choice for volumetry as long as it is reproducible and robust. Thus robust algorithm that produces more reproducible/consistent results than existing more accurate but less robust solutions can be a better choice in this application context.

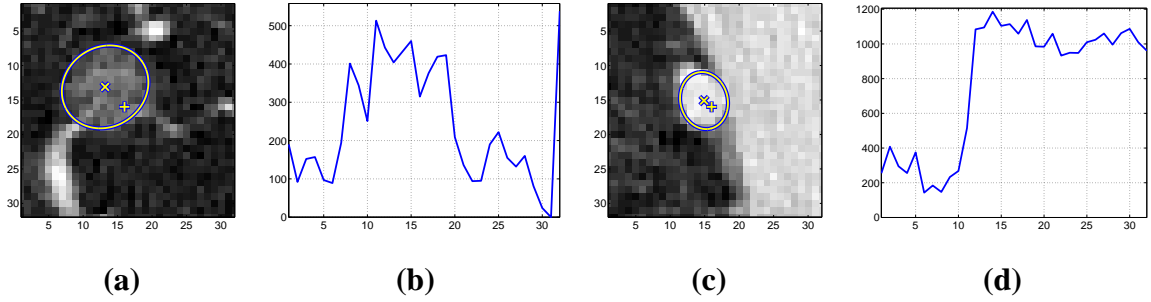


Figure 1: An illustration of pulmonary nodule examples with typical data noises captured in 3D CT images. From left to right, (a): vascularized pure GGN, (b): 1D vertical profile of (a). (c): nodule attached to pleural surface in 2D dissection, and (d): 1D horizontal profile of (c) through the nodule center, The voxel-intensities in (b,d) indicate the Hounsfield unit with an offset 1024. “+” denotes markers used as initialization points provided by expert radiologists. The estimated nodule center and anisotropic spread are shown by “x” and 35% confidence ellipses, respectively.

1.8 GGN Characterization: Our Approach

Robust anisotropic Gaussian fitting (RAGF) algorithm proposed by our previous work [45, 46] is one example of such robust nodule segmentation solution. Instead of finding an accurate nodule boundary estimate, RAGF algorithm addresses *nodule characterization problem*, yielding a robust estimate of ellipsoidally approximated nodule boundary and a set of nodule characterizations in terms of i) nodule center, ii) nodule volume, iii) maximum diameter, iv) average diameter, and v) isotropy. The algorithm is designed to be robust against the real CT data with noise that is intrinsic to the measurement process and also the pathology and anatomy of our interest, including the variability of GGNs,

1. deviation of the signal from a Gaussian intensity model of our choice (i.e., non-Gaussianity: Fig.1(a,b)),
2. uncertainty in the marker location “+” given by system users (i.e., initialization: Fig.1(a,c)), and
3. influences from surrounding structures such as the pleural surface and vessels (i.e., margin-truncation: Fig.1(c,d)).

Fig.1 illustrates two example cases in 2D cross-sectional and 1D profile views of the two lesions for the pure GGN and the juxtapleural case [29]. The RAGF method succeeds in robustly approximating the nodule boundary (shown by the solid-line ellipses around the center \mathbf{x} in the figure) and its volumetric measurements even with the presence of these difficulties. The algorithm is relevant to the GGN characterization because not only it is robust against GGNs' variable intensity appearances but also it can handle the cases with pleural surfaces since small peripheral adenocarcinoma has high likelihood for such wall-attachments. An extensive validation study with 1310 cases has demonstrated this method's effectiveness for solitary pulmonary nodules in both primary and secondary lung cancers. However its effectiveness for GGN cases has not been fully confirmed by our previous studies. In this chapter, we validate the same RAGF algorithm proposed in [46] with a dataset of 56 GGN cases. The rest of this chapter presents the summary of the RAGF algorithm, as well as the results of the experimental validation.

2 Methods: RAGF Nodule Characterization

The pulmonary nodule in a chest CT image typically appears as a local concentration of high CT values surrounded by very low CT values of lung parenchyma as background. One of the most common model functions for describing the characteristics of such bounded signals is the Gaussian function [34, 46].

The volumetric CT image is treated as the discretization of a $d(=3)$ -dimensional continuous non-negative signal $f(\mathbf{x})$ over a 3D regular lattice. The non-positiveness is assured by using the offset with 1024 to the CT values in Hounsfield unit. The symbol \mathbf{u} is used for describing the location of a spatial local maximum of f . Suppose that the local region of f around \mathbf{u} can be *approximated* by a product of a d -variate Gaussian function and a positive multiplicative parameter,

$$f(\mathbf{x}) \simeq \alpha \times [\Phi(\mathbf{x}; \mathbf{u}, \Sigma)]_{\mathbf{x} \in \mathcal{S}} \quad (1)$$

$$\Phi(\mathbf{x}; \mathbf{u}, \Sigma) = (2\pi)^{-d/2} |\Sigma|^{-1/2} \exp\left(-\frac{1}{2}(\mathbf{x} - \mathbf{u})^t \Sigma^{-1} (\mathbf{x} - \mathbf{u})\right) \quad (2)$$

where \mathcal{S} is a set of data points in the neighborhood of \mathbf{u} , belonging to the *basin of attraction* of \mathbf{u} . The problem of our interest can now be understood as the parametric model fitting and

the estimation of the model parameters: mean \mathbf{u} , covariance Σ , and amplitude α . The *mean* and *covariance* of Φ describe the *spatial local maximum* and *spread* of the nodule appearance, respectively.

As discussed in the previous section, the above assumption for choosing the Gaussian intensity model can be largely violated when applied to GGN cases since the intensity distribution of GGNs will most likely not follow that of a Gaussian function (See Fig.1(b)). Two approaches can be pursued in this situation. The first is to choose a model that better fits the data. This is a difficult approach since formulating a functional model that covers all possible GGN appearances is a challenging task. Instead, we take the second approach of devising a robust model-fitting/parameter-estimation scheme, which allows the fit of a model to data that do not closely follow the model assumption. The following sections describe one such example by combining the ideas from robust non-parametric density estimation and scale-space data analysis.

2.1 Theory: Anisotropic Scale-Space and Scale-Space Mean Shift

The scale-space theory [62, 28, 38] states that, given any d -dimensional continuous signal $f : \mathbb{R}^d \rightarrow \mathbb{R}$, the scale-space representation $F : \mathbb{R}^d \times \mathbb{R}_+ \rightarrow \mathbb{R}$ of f is defined to be the solution of the diffusion equation, $\partial_h F = 1/2 \nabla^2 F$, or equivalently the convolution of the signal with Gaussian kernels $\Phi(\mathbf{x}; \mathbf{0}, \mathbf{H})$ of various bandwidths (or scales) $\mathbf{H} \in \mathbb{R}^{d \times d}$,

$$F(\mathbf{x}; \mathbf{H}) = f(\mathbf{x}) * \Phi(\mathbf{x}; \mathbf{0}, \mathbf{H}). \quad (3)$$

When $\mathbf{H} = h\mathbf{I}$ ($h > 0$), F represents the solution of the isotropic diffusion process [38]. When \mathbf{H} is allowed to be a fully-parameterized symmetric positive definite matrix, F represents *anisotropic scale-space* that is the solution to a partial differential equation: $\partial_{\mathbf{H}} F = 1/2 \nabla \nabla^t F$.

The gradient vector of the anisotropic scale-space representation $F(\mathbf{x}; \mathbf{H})$ can be written as convolution of f with the Gaussian derivative kernel $\nabla \Phi$, since the gradient operator commutes across the convolution operation. Some algebra reveals that ∇F can be expressed as a function of

a vector whose form resembles the fixed-bandwidth density mean shift [7],

$$\begin{aligned}
\nabla F(\mathbf{x}; \mathbf{H}) &= f(\mathbf{x}) * \nabla \Phi(\mathbf{x}; \mathbf{H}) \\
&= \int f(\mathbf{x}') \Phi(\mathbf{x} - \mathbf{x}'; \mathbf{H}) \mathbf{H}^{-1}(\mathbf{x}' - \mathbf{x}) d\mathbf{x}' \\
&= \mathbf{H}^{-1} \int \mathbf{x}' \Phi(\mathbf{x} - \mathbf{x}'; \mathbf{H}) f(\mathbf{x}') d\mathbf{x}' - \mathbf{H}^{-1} \mathbf{x} \int \Phi(\mathbf{x} - \mathbf{x}'; \mathbf{H}) f(\mathbf{x}') d\mathbf{x}' \\
&= \mathbf{H}^{-1} F(\mathbf{x}; \mathbf{H}) \mathbf{m}(\mathbf{x}; \mathbf{H})
\end{aligned} \tag{4}$$

$$\mathbf{m}(\mathbf{x}; \mathbf{H}) \equiv \frac{\int \mathbf{x}' \Phi(\mathbf{x} - \mathbf{x}'; \mathbf{H}) f(\mathbf{x}') d\mathbf{x}'}{\int \Phi(\mathbf{x} - \mathbf{x}'; \mathbf{H}) f(\mathbf{x}') d\mathbf{x}'} - \mathbf{x}. \tag{5}$$

Eq.(5) defines *scale-space mean shift*: the extended fixed-bandwidth mean shift vector for f . Eq.(5) can be seen as introducing a weight variable $w \equiv f(\mathbf{x}')$ to the kernel $K(\mathbf{x}') \equiv \Phi(\mathbf{x} - \mathbf{x}')$. Therefore, an arithmetic mean of \mathbf{x}' is weighted by the product of the kernel and signal values $K'(\mathbf{x}') \equiv \Phi(\mathbf{x} - \mathbf{x}')f(\mathbf{x}')$. The mean shift procedure [8] is defined as iterative updates of a data point \mathbf{x}_i until its convergence at \mathbf{y}_i^m ,

$$\mathbf{y}_{j+1} = \mathbf{m}(\mathbf{y}_j; \mathbf{H}) + \mathbf{y}_j; \quad \mathbf{y}_0 = \mathbf{x}_i. \tag{6}$$

Such iteration gives a robust and efficient algorithm of gradient-ascent, since $\mathbf{m}(\mathbf{x}; \mathbf{H})$ can be interpreted as a normalized gradient by rewriting Eq.(4); $\mathbf{m}(\mathbf{x}; \mathbf{H}) = \mathbf{H} \nabla F(\mathbf{x}; \mathbf{H}) / F(\mathbf{x}; \mathbf{H})$. The direction of the mean shift vector aligns with the exact gradient direction when \mathbf{H} is isotropic with a positive scale.

2.2 Robust Gaussian Mean Estimation

We assume that the 3D volume is given with information of where the target structure is roughly located but we do not have explicit knowledge of its spread. The marker point \mathbf{x}_p indicates such location information. We allow \mathbf{x}_p to be placed anywhere within the basin of attraction \mathcal{S} of the target structure. In this condition, the Gaussian mean \mathbf{u} can be estimated as a local intensity mode of the scale-space with a fixed bandwidth \mathbf{H} by using the mean shift procedure in Eq.(6) with \mathbf{x}_p as its initial point. To increase the robustness of this approach, we run N_1 mean shift procedures initialized by sampling the neighborhood of \mathbf{x}_p uniformly. The majority of the procedure's conver-

gence at the same location (in terms of the Mahalanobis distance with \mathbf{H}) indicates the location of the maximum.

2.3 Robust Gaussian Covariance Estimation

The Gaussian covariance Σ in Eq.(1) characterizes the d -dimensional anisotropic spread and orientation of the signal f around the estimated mode \mathbf{u} . It can be robustly estimated by using information only sampled within the basin of attraction of the target nodule, ignoring the information that belongs to other structures. This is done by collecting mean shift vectors along convergent scale-space mean shifts from multiple seed points then estimating the unknown covariance as a function of the collected mean shifts by solving a constrained least-squares problem.

With the signal model of Eq.(1), the definition of the mean shift vector of Eq.(5) can be rewritten as a function of Σ ,

$$\begin{aligned} \mathbf{m}(\mathbf{y}_j; \mathbf{H}) &= \mathbf{H} \frac{\nabla F(\mathbf{y}_j; \mathbf{H})}{F(\mathbf{y}_j; \mathbf{H})} \\ &\simeq \mathbf{H} \frac{\alpha \Phi(\mathbf{y}_j; \mathbf{u}, \Sigma + \mathbf{H})(\Sigma + \mathbf{H})^{-1}(\mathbf{u} - \mathbf{y}_j)}{\alpha \Phi(\mathbf{y}_j; \mathbf{u}, \Sigma + \mathbf{H})} \\ &= \mathbf{H}(\Sigma + \mathbf{H})^{-1}(\mathbf{u} - \mathbf{y}_j). \end{aligned} \quad (7)$$

Further rewriting Eq.(7) results in a linear matrix equation of unknown Σ ,

$$\Sigma \mathbf{H}^{-1} \mathbf{m}_j = \mathbf{b}_j \quad (8)$$

where $\mathbf{m}_j \equiv \mathbf{m}(\mathbf{y}_j; \mathbf{H})$ and $\mathbf{b}_j \equiv \mathbf{u} - \mathbf{y}_j - \mathbf{m}_j$. An over-complete set of the linear equations can be formed by using all the trajectory points $\{\mathbf{y}_j | j = 1, \dots, t_u\}$ that converge to the same \mathbf{u} located within the basin of attraction \mathcal{S} . For efficiently collecting a sufficient number of samples $\{(\mathbf{y}_j, \mathbf{m}_j)\}$, we run N_2 mean shift procedures initialized by sampling the neighborhood of pre-estimated \mathbf{u} uniformly. This results in t_u samples ($t_u = \sum_{i=1}^{N_2} t_i$), where t_i denotes the number of points on the convergent trajectory starting from \mathbf{x}_i . The system described in Eq.(8) can be

formulated as a constrained least-squares problem,

$$\begin{aligned}
\mathbf{A}\Sigma &= \mathbf{B} \\
\Sigma &\in \mathcal{SPD} \\
\mathbf{A} &= (\mathbf{m}_1, \dots, \mathbf{m}_{t_u})^t \mathbf{H}^{-t} \\
\mathbf{B} &= (\mathbf{b}_1, \dots, \mathbf{b}_{t_u})^t
\end{aligned} \tag{9}$$

where \mathcal{SPD} denotes a set of symmetric positive definite matrices in $\mathbb{R}^{d \times d}$. The unique closed-form solution Σ^{**} of this system is given by

$$\Sigma^{**} = \mathbf{U}_P \Sigma_P^{-1} \mathbf{U}_{\tilde{Q}} \Sigma_{\tilde{Q}} \mathbf{U}_{\tilde{Q}}^t \Sigma_P^{-1} \mathbf{U}_P^t \tag{10}$$

which involves symmetric Schur decompositions [16, p.393] of the matrices $\mathbf{P} \equiv \mathbf{A}^t \mathbf{A}$ and $\tilde{\mathbf{Q}} \equiv \Sigma_P \mathbf{U}_P^t \mathbf{Q} \mathbf{U}_P \Sigma_P$ given $\mathbf{Q} \equiv \mathbf{B}^t \mathbf{B}$, i.e.,

$$\begin{aligned}
\mathbf{P} &= \mathbf{U}_P \Sigma_P^2 \mathbf{U}_P^t \\
\tilde{\mathbf{Q}} &= \mathbf{U}_{\tilde{Q}} \Sigma_{\tilde{Q}}^2 \mathbf{U}_{\tilde{Q}}^t.
\end{aligned}$$

The solution Σ^{**} is derived from finding \mathbf{Y}^{**} in the Cholesky factorization of $\Sigma = \mathbf{Y}\mathbf{Y}^t$. It can be shown that Σ^{**} uniquely minimizes an area criterion $\|\mathbf{A}\mathbf{Y} - \mathbf{B}\mathbf{Y}^{-t}\|_F^2$ where $\|\cdot\|_F$ denotes the Frobenius norm.

2.4 Robust Scale Selection

The previous sections explain how the RAGF method estimates the Gaussian center \mathbf{u} and spread Σ given an analysis bandwidth \mathbf{H} . The scale-space-based multi-scale analysis treats \mathbf{H} as a variable parameter. Our procedure repeats the Gaussian fitting for a set of analysis bandwidths $\{\mathbf{H}_k | k = 1, \dots, K\}$. Then the bandwidth that provides the optimal among K estimates is sought by a certain criterion. RAGF algorithm exploits the stability test proposed in [7]. Given a set of estimates $\{(\mathbf{u}_k, \Sigma_k)\}$ for a series of the successive linear analysis bandwidths $\{h_k | k = 1, \dots, K\}$, a form of the Jensen-Shannon divergence is defined by,

$$JS(k) = \frac{1}{2} \log \frac{|\frac{1}{2a+1} \sum_{i=k-a}^{k+a} \Sigma_i|}{\sqrt[2a+1]{\prod_{i=k-a}^{k+a} |\Sigma_i|}} + \frac{1}{2} \sum_{i=k-a}^{k+a} (\mathbf{u}_i - \mathbf{u})^t \left(\sum_{i=k-a}^{k+a} \Sigma_i \right)^{-1} (\mathbf{u}_i - \mathbf{u}) \tag{11}$$

where $\mathbf{u} = \frac{1}{2a+1} \sum_{k-a}^{k+a} \mathbf{u}_i$ and a define the neighborhood width of the divergence computation. The most stable estimate across the analysis bandwidths provides a local minimum of the divergence profile. We treat the minimizer as the final estimation of the RAGF method (\mathbf{u}^*, Σ^*) .

2.5 Algorithm Overview

The RAGF algorithm assumes that a marker indicating the rough location of the target nodule is given *a priori*. Such information can be provided by a user of a GUI-based system. The estimation algorithm is presented below.

Problem Given the 3D input data $f(\mathbf{x})$, a marker point \mathbf{x}_p , a set of analysis scales $\{\mathbf{H}_k | k = 1, \dots, K\}$, estimate the 3D anisotropic structure of a nodule (\mathbf{u}^*, Σ^*) .

Scale-specific estimation For each k ,

1. Perform uniform sampling centered at x_p , resulting in a set of N_1 starting points.
2. Perform the mean shift procedure in Eq.(6) from each starting point.
3. Take the convergence point of the majority of the points as the location estimate \mathbf{u}_k .
4. Perform uniform sampling centered at \mathbf{u}_k , resulting in a set of N_2 starting points.
5. Perform the mean shift procedure from each starting point.
6. Construct the system in Eq.(9) with the mean shift vectors $\{\mathbf{m}(\mathbf{y}_j)\}$ along the converging trajectories.
7. Solve the system by Eq.(10), resulting in the covariance estimate Σ_k .

Scale selection With K estimates $\{(\mathbf{u}_k, \Sigma_k)\}$,

1. Compute the divergence $\{JS(\mathbf{u}_k, \Sigma_k)\}$ using Eq.(11) for $k = 1 + a, \dots, K - a$.
2. Find the most stable solution (\mathbf{u}^*, Σ^*) by finding a local minimum of $\{JS_k\}$: $\operatorname{argmin}_k JS(\mathbf{u}_k, \Sigma_k)$.

2.6 Volumetric Measurements

The multi-scale Gaussian-based model fitting, described in the previous sections, results in the mean and covariance estimates (\mathbf{u}^*, Σ^*) of a Gaussian function that fits the given data best. Treating the fitted model as a normal probability distribution $\mathcal{N}(\mathbf{x}; \mathbf{u}^*, \Sigma^*)$, the tumor boundary segmentation can be approximated by a confidence ellipsoid forming a 3D equal-probability contour. Such a confidence ellipsoid is defined by the solutions to the following generic quadratic equation,

$$(\mathbf{x} - \mathbf{u}^*)^t \Sigma^{*-1} (\mathbf{x} - \mathbf{u}^*) = \sigma^2 \quad (12)$$

where σ^2 is a squared Mahalanobis distance, defining the confidence limit. The volumetry of an ellipsoid can be determined as a function of three radii along its major and two minor orthogonal axes. The radii are denoted by $r_i > 0$ ($r_1 \geq r_2 \geq r_3$).

The following derives r_i from the eigen decomposition of the covariance Σ^* . Such eigen decomposition can be expressed in a matrix equation: $\Sigma^* \mathbf{V} = \mathbf{V} \mathbf{L}$. \mathbf{V} is a column matrix of the eigenvectors \mathbf{v}_i and \mathbf{L} is a diagonal matrix of the corresponding eigenvalues λ_i^2 ($\lambda_1 \geq \lambda_2 \geq \lambda_3$). Right-multiply the matrix equation with \mathbf{V}^t yields the symmetric Schur decomposition of Σ^* : $\Sigma^* = \mathbf{V} \mathbf{L} \mathbf{V}^t$. Since $\Sigma^{*-1} = \mathbf{V} \mathbf{L}^{-1} \mathbf{V}^t$, with a coordinate transform $\mathbf{y} \equiv \mathbf{V}^t (\mathbf{x} - \mathbf{u}^*)$, Eq.(12) can be simplified to: $\mathbf{y}^t \mathbf{L}^{-1} \mathbf{y} = \sigma^2$. Substituting three points, $\mathbf{y} = (r_1, 0, 0)^t, (0, r_2, 0)^t, (0, 0, r_3)^t$, which are known to lie on the ellipsoid surface, to the quadratic equation results in,

$$r_i = \sigma \lambda_i \quad (13)$$

As a result, the following volumetric measurement formulae can immediately be derived for the volume $V = \frac{4}{3} \pi \sigma^3 \prod_i \lambda_i$, the maximum diameter $L = 2\sigma \lambda_1$, the average diameter $A = \frac{2}{3} \sigma \sum_i \lambda_i$, and the isotropy $R = \frac{\lambda_2 + \lambda_3}{2\lambda_1}$, where V , L , and A are in the voxel unit and the isotropy R ranges in $[0, 1]$, taking the value 1 when it becomes a sphere. The bias of these volumetric measurements are caused solely by the segmentation error. Therefore, these formulae are exact thus free from the partial volume effect when the tumor boundary is well-characterized by the ellipsoidal segmentation.

Given a voxel dimension in a physical unit, the volumetric measurement formulae above can be revised to produce the measurements in the unit. This is a crucial step for any comparative

and differential studies because the voxel dimension can vary across different scans. Suppose that a voxel dimension is given as $(\Delta x, \Delta y, \Delta z)$ in millimeter or any other unit. After a coordinate transform, eigenvalues in the unit of millimeter, λ'_i , can be expressed as a function of the voxel dimensions and eigenvectors,

$$\lambda'_i = \beta_i \lambda_i \quad (14)$$

$$\beta_i = \sqrt{(v_{xi}\Delta x)^2 + (v_{yi}\Delta y)^2 + (v_{zi}\Delta z)^2} \quad (15)$$

where the eigenvector is denoted by $\mathbf{v}_i = (v_{xi}, v_{yi}, v_{zi})^t$. This leads us to the following formulae which takes the voxel dimension into account,

$$V' = \frac{4}{3}\pi\sigma^3 \prod_i \beta_i \lambda_i \quad (16)$$

$$L' = 2\sigma \lambda'_1 = 2\sigma \max_i \beta_i \lambda_i \quad (17)$$

$$A' = \frac{2}{3}\sigma \sum_i \beta_i \lambda_i \quad (18)$$

$$R' = \frac{\lambda'_2 + \lambda'_3}{2\lambda'_1} \quad (19)$$

where $\lambda'_1 \geq \lambda'_2 \geq \lambda'_3$. Note that λ'_i must be re-sorted from the original order given by the eigen decomposition because the coordinate transform may change such an order.

3 Experiments

3.1 Data

A dataset of 56 clinical GGN cases is used in this study. Thin-section chest high-resolution computed tomography (HRCT) images of 34 patients are recorded by multiple multislice CT scanners (Somatom Volume Zoom and Somatom Sensation 16; Siemens) and anonymized. Each volumetric image consists of 12-bit positive values over an array of 512x512 lattices. The number of slices in a CT volume and the dimensions of a voxel vary across volumes in our data set. The number of slices ranges between 217 and 616. The voxel dimensions range within

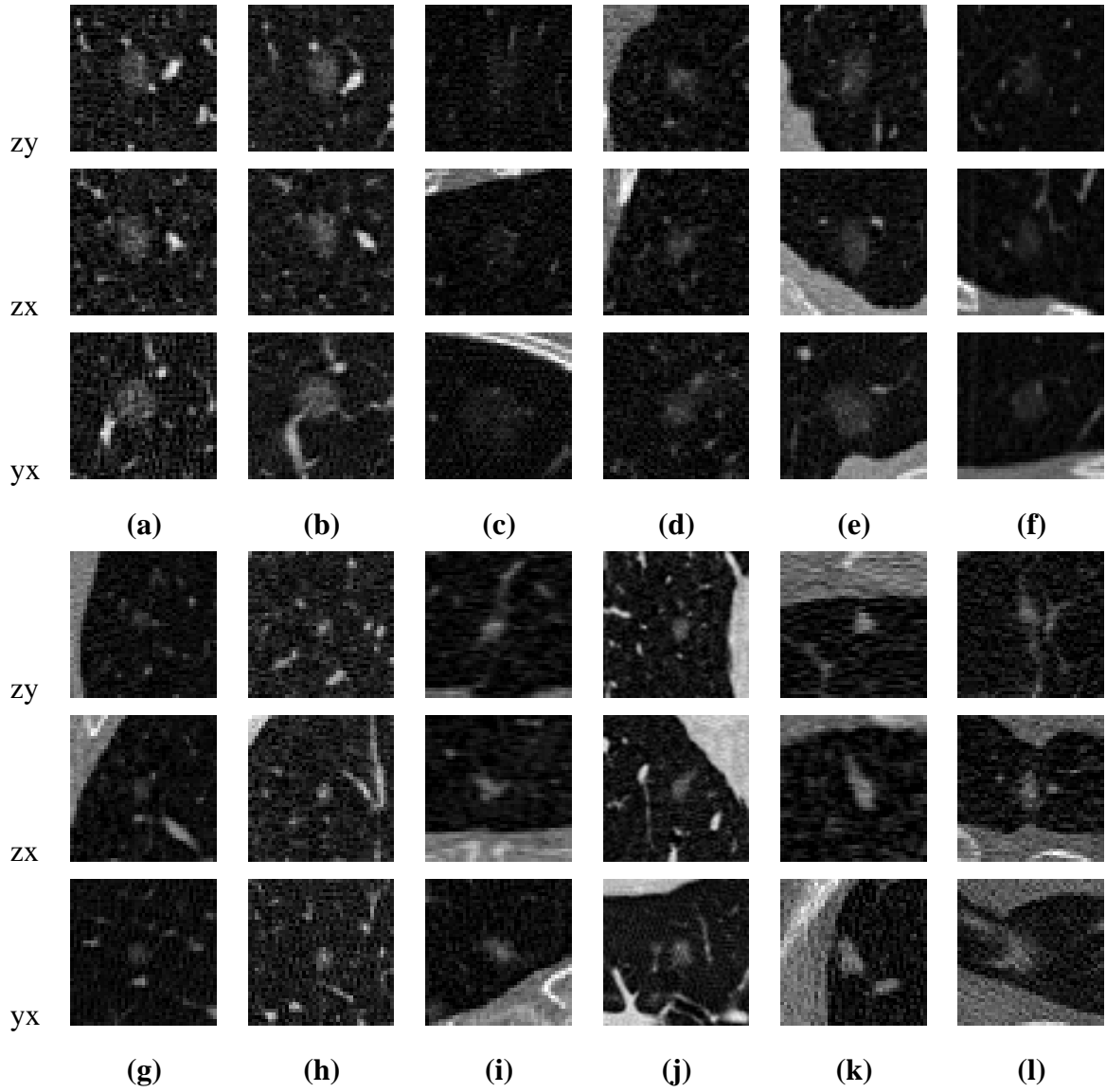


Figure 2: Twelve GGN examples in 3D HRCT. Each case is shown in the three-plane MPR view of a 43-voxel cubic volume-of-interest. Cases (a-b) are circular, cases (c-f) are with hazy opacity, cases (g-j) are small (<5mm), and cases (k-l) are attached to pleural surface.

[0.4609 – 0.8281, 0.4609 – 0.8281, 0.5 – 1] in millimeter. Fifty-six GGN lesions were identified by trained radiologists among the set of volumes. For each GGN lesion, the radiologists provided the initialization marker \mathbf{x}_p indicating its rough location and a 43-voxel cubic volume-of-interest (VOI) centered at the marker is extracted as a pre-process. All cases are small (<15mm) and 44 of them are extremely small (<5mm). Thirty-nine cases are peripheral located near or attached to the lung wall. Fig. 2 shows 12 illustrative examples of this dataset with circular (a-b), hazy (c-f), and small (g-j), and attached (k-l) cases.

3.2 Results

A 3D implementation of the RAGF algorithm is evaluated with the above GGN dataset. The implementation is straightforward without any 3D specific adaptation. The analysis bandwidths are set to 18 scales with 0.25 interval $h = (0.50^2, 0.75^2, \dots, 4.75^2)$. Uniform sampling in the 3-voxel neighborhood of the marker (i.e., $N_1 = 7$) is used for estimating local maximum. The 3-voxel size is determined empirically. The same strategy is employed for initializing the mean shift trajectories around the local maximum (i.e., $N_2 = 7$). The neighborhood width of the divergence computation is set to $a = 1$ (considering only three adjacent scales).

Fig. 3 displays the results of the RAGF method for one GGN example case (Fig.2(a)). The second row shows the intensity images generated from the Gaussian model fitted to the data in the first row. The third row shows the result of approximated nodule boundary shown as 2D intersections of the 35% confidence ellipsoid of the fitted Gaussian. Fig. 4 shows the RAGF characterization results for the examples shown in Fig. 2. Our visual inspection revealed that the marker locations provided by trained radiologists are noticeably off-centered in many cases, deviating from the true/estimated nodule centers with a certain degree. The correct estimations for these GGN cases demonstrate the feasibility and effectiveness of the RAGF method for GGN characterization.

Next the quantitative performance of the RAGF with the above dataset is studied. Due to the lack of ground-truth for 3D nodule segmentation, the classification of the correct or failure estimation is given manually by eye-appraisal of experts using a 3D render view and its corresponding

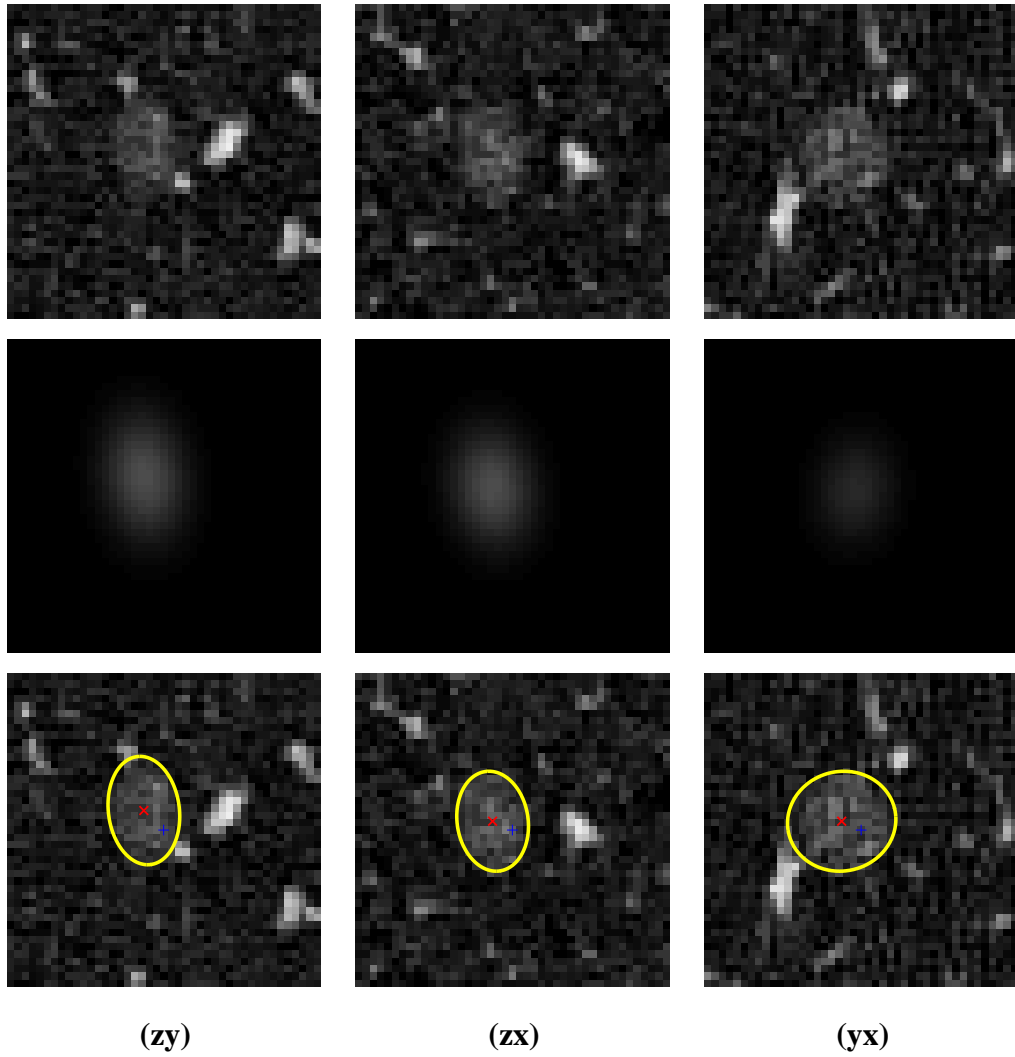


Figure 3: An example of nodule characterization by the RAGF algorithm. A circular GGN example in Fig. 2(a) is shown in the first row. The second row shows the estimated intensity image of the Gaussian model fitted to the above data by the RAGF. The third row shows the final nodule boundary approximation by the 35% confidence ellipsoid of the fitted Gaussian. The marker locations are indicated by +. The estimated nodule centers are indicated by x.

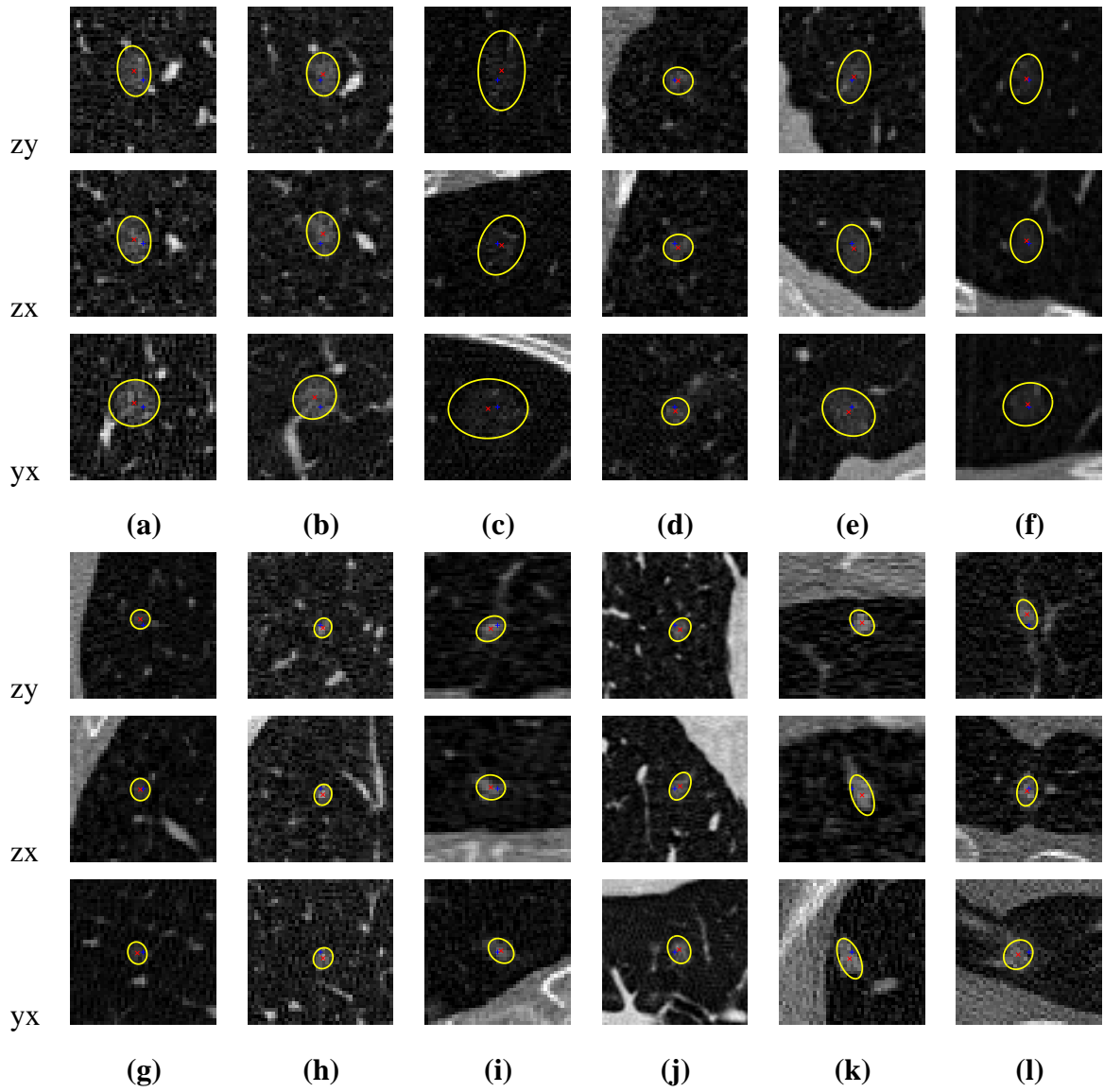


Figure 4: Nodule characterization results by the RAGF algorithm for the twelve GGN examples shown in Fig. 2. See captions of Fig.3 and Fig.2 for details

Estimation	# Cases (%)	Verification	# Cases (%)
Correct	49 (87.5)	TP	44 (78.6)
		FN	5 (8.9)
Failure	7 (12.5)	TN	4 (7.1)
		FP	3 (5.4)

Table 1: Quantitative performance evaluation of the RAGF method. The data set consists of 56 pure GGNs from 34 patients. Multiple scanners are used for data collection. TP: true positive, accepted correct estimates. FN: false negative, rejected correct estimates. TN: true negative, rejected false estimates. FP: false positive, accepted false estimates.

MPR view. Statistical verification using the chi-square test [46] is also performed for each RAGF result to determine whether to accept or reject it.

Table 1 summarizes the resulting performance statistics. 49 cases (87.5%) resulted in successful nodule characterization confirmed by the eye-appraisal. For verification, small percentage of cases resulted in false acceptance (3 false positives (FPs): 5.4%) and false rejection (5 false negatives (FNs): 8.9%). The few failures were caused by a) under-segmentation due to nearby vessels (two FPs and one TN), b) mis-detection due to wall-attachment (two TNs), c) over-segmentation due to very hazy opacity (one TN), and d) under-segmentation due to necrosis (one FP). Fig. 5 shows examples for these four causes of failures. Fig. 5(a) illustrates the failure due to nearby vessels. The RAGF in this case captures a small high-intensity vessel region rather than the GGN attached to the vessel. This case corresponds to a failure of the scale selection process which mistakenly chose the analysis scale that corresponds to the vessel to be most stable. Fig. 5(b) illustrates the case where a GGN attached to the lung wall is missed. This failure was mainly caused by ill-placed markers. With such markers, non-pathological structures nearby the markers can be characterized instead of the target nodule and are accidentally well-approximated by the Gaussian distribution (e.g., rib bones). 37 other peripheral cases were correctly characterized. Fig. 5(c) shows the failure where the opacity of GGN is so low that the RAGF’s covariance estimation failed. Finally, Fig. 5(d) shows a case with necrosis inside of a GGN. In such a case, the nodule center exhibits a hollow, causing the RAGF to capture a sub-region of the target GGN. Overall,

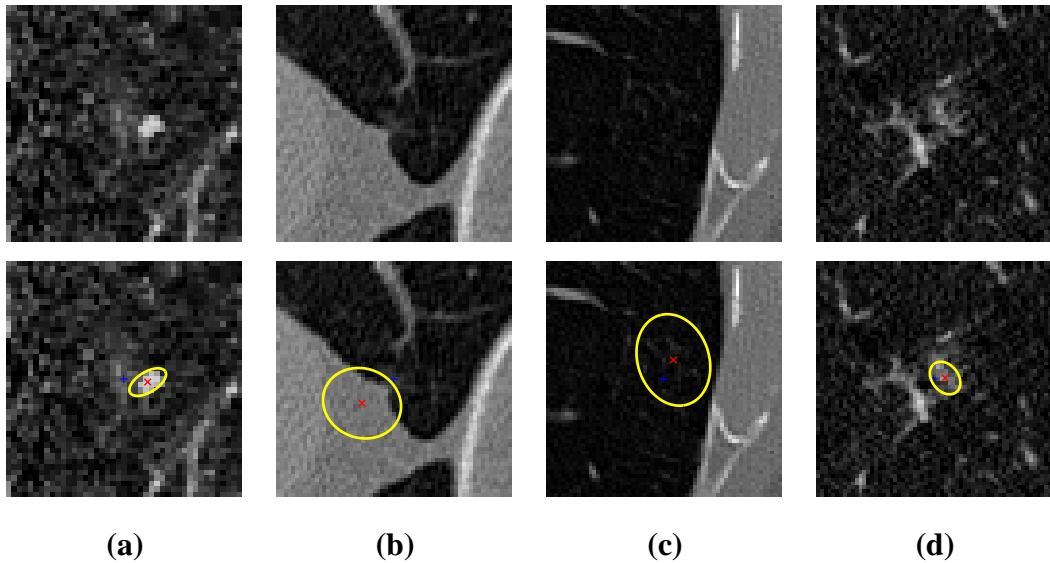


Figure 5: Examples of failures by the RAGF algorithm. (a) under-segmentation due to nearby vessels, (b) mis-detection due to wall-attachment, (c) over-segmentation due to very hazy opacity, (d) under-segmentation due to necrosis.

the majority of the GGN cases were correctly characterized except for these special cases and the results were successfully verified for acceptance or rejection.

4 Conclusion

This chapter presents a comprehensive literature review of GGNs across the fields of radiology, pathology, medical image analysis, and an experimental evaluation of the RAGF nodule characterization method with a clinical dataset with 56 pure GGN cases. GGN is a fairly new subject in all these interdisciplinary fields because we have come to some understanding of them only after the recent advent of the high-resolution CT technologies. While there exist a number of clinical and technical reviews of this subject in the literature, to the best of our knowledge, this is the first to offer a comprehensive review of this subject under these related disciplines together.

The RAGF algorithm was originally proposed as a robust nodule characterization solution for arbitrary types of nodules. Although the original report addressed a potential advantage of the

method to some GGN cases, no systematic evaluation of the method's effectiveness toward GGN was performed to date. This chapter presents the first experimental validation of the RAGF with the clinical dataset, demonstrating the feasibility of the method in the GGN application. Note that the RAGF's original performance with a large clinical data set of 1310 nodules resulted in 81.2% success rate. With our GGN dataset, the same RAGF algorithm resulted in 87.5% success rate. The voxel intensity distribution of the GGNs are much more irregular than the typical solid nodules. The favorable performance of the RAGF with GGNs indicates that it is indeed capable to robustly characterize a wide range of nodule types, including these pure GGNs.

As our future work, we plan to improve the performance of the RAGF method for the cases attached to lung walls and vessels (Fig.5(a,b)) in order to improve the performance further. For deriving more clinically conclusive result, we plan to evaluate more GGN cases, especially the mixed cases, as well as to evaluate actual volumetry from follow-up CT data.

Overall, the presented RAGF method is generic and does not depend on semantics of the absolute CT values in the Hounsfield unit. The robustness, flexibility, and efficiency of the proposed framework, therefore, facilitates not only the pulmonary nodule applications in CT sought in this chapter but also various other applications in different imaging domains (e.g., PET scans) and different pathological and anatomical structures (e.g., polyps), involving with the analysis of blob-like geometrical structures. We plan to explore such other applications of our method in future.

Acknowledgments

The author wishes to thank Dorin Comaniciu, Arun Krishnan, Senthil Periaswamy, Toshiro Kubota, Marcos Salganicoff, Visvanathan Ramesh, and Alok Gupta for their support and stimulating discussions.

References

- [1] T. Aoki, H. Nakata, H. Watanabe, K. Nakamura, T. Kasai, H. Hashimoto, and et al., “Evolution of peripheral lung adenocarcinomas: CT findings correlated with histology and tumor doubling time,” *AJR Am J Roentgenol*, vol. 174, p. 7638, 2000.
- [2] T. Aoki, Y. Tomoda, H. Watanabe, H. Nakata, T. Kasai, H. Hashimoto, M. Kodate, T. Osaki, and K. Yasumoto, “Peripheral lung adenocarcinoma: Correlation of thin-section CT findings with histologic prognostic factors and survival,” *Radiology*, vol. 220, pp. 803–809, 2001.
- [3] H. Ashraf, B. de Hoop, S. B. Shaker, A. Dirksen, K. S. Bach, H. Hansen, M. Prokop, and J. H. Pedersen, “Lung nodule volumetry: segmentation algorithms within the same software package cannot be used interchangeably.” In press, 2010.
- [4] H. Bastawrous, N. Nitta, and M. Tsudagawa, “A new CAD system for detecting localized ground glass opacity nodules in lung CT images using cross and coronary section images,” in *Int. Workshop Med. Measurement and Applications*, (Benevento), 2006.
- [5] W. A. Browder, A. P. Reeves, T. Apananosovich, M. Cham, D. F. Yankelevitz, and C. I. Henschke, “Automated volumetric segmentation method for growth consistency of nonsolid pulmonary nodules in high-resolution CT,” in *SPIE*, volume 6514, 2007, pp. 1709–1719.
- [6] L. Cardinale, F. Ardisson, S. Novello, M. Busso, F. Solitro, M. Longo, D. Sardo, M. Giors, and C. Fava, “The pulmonary nodule: clinical and radiological characteristics affecting diagnosis of malignancy,” *Radiol med*, vol. 114, pp. 871–889, 2009.
- [7] D. Comaniciu, “An algorithm for data-driven bandwidth selection,” *IEEE Trans. Pattern Anal. Machine Intell.*, vol. 25, no. 2, pp. 281–288, 2003.
- [8] D. Comaniciu and P. Meer, “Mean shift: A robust approach toward feature space analysis,” *IEEE Trans. Pattern Anal. Machine Intell.*, vol. 24, no. 5, pp. 603–619, 2002.
- [9] S. Diederich, “Pulmonary nodules: do we need a separate algorithm for non-solid lesions?,” *Cancer Imaging*, vol. 9, pp. S126–S128, 2009.
- [10] T. Ezoe, H. Takizawa, S. Yamamoto, A. Shimizu, T. Matsumoto, Y. Tateno, T. Iimura, and M. Matsumoto, “Automatic detection method of lung cancers including ground-glass opacities from chest x-ray CT images,” in *SPIE*, volume 4684, 2002, pp. 1672–1680.

- [11] F. Fischback, F. Knollmann, V. Griesshaber, T. Freund, E. Akkol, and R. Felix, "Detection of pulmonary nodules by multislice computed tomography: improved detection rate with reduced slice thickness," *Eur. Radiol.*, vol. 13, pp. 2378–2383, 2003.
- [12] M. Gaeta, R. Caruso, M. Barone, S. Volta, G. Casablanca, and F. La Spada, "Ground-glass attenuation in nodular bronchioloalveolar carcinoma: Ct patterns and prognostic value," *J Comput Assist Tomogr*, vol. 22, pp. 215–219, 1998.
- [13] M. A. Gavrielides, L. M. Kinnard, K. J. Myers, and N. Petrick, "Noncalcified lung nodules: Volumetric assessment with thoracic CT," *Radiology*, vol. 251, p. 2639, 2004.
- [14] M. Godoy and D. Naidich, "Subsolid pulmonary nodules and the spectrum of peripheral adenocarcinomas of the lung: Recommended interim guidelines for assessment and management," *Radiology*, vol. 253, pp. 606–622, 2009.
- [15] J. Goldin, M. Brown, and I. Petkovska, "Computer-aided diagnosis in lung nodule assessment," *J Thorac Imaging*, vol. 23, pp. 97–104, 2008.
- [16] G. H. Golub and C. F. van Loan, *Matrix Computations*. Baltimore: Johns Hopkins University Press, 1996.
- [17] J. M. Goo, T. Tongdee, R. Tongdee, K. Yeo, C. F. Hildebolt, and K. T. Bae, "Volumetric measurement of synthetic lung nodules with multi-detector row CT: effect of various image reconstruction parameters and segmentation thresholds on measurement accuracy," *Radiology*, vol. 235, p. 850856, 2005.
- [18] P. A. Hein, V. C. Romano, P. Rogalla, C. Klessen, A. Lembcke, L. Bornemann, V. Dicken, B. Hamm, and H. C. Bauknecht, "Variability of semiautomated lung nodule volumetry on ultralow-dose CT: comparison with nodule volumetry on standard-dose CT," *J Digital Imaging*, vol. 23, pp. 8–17, 2010.
- [19] C. I. Henschke, D. F. Yankelevitz, R. Mirtcheva, G. McGuinness, D. McCauley, and O. S. Miettinen, "CT screening for lung cancer: frequency and significance of part-solid and non-solid nodules," *AJR Am. J. Roentgenol.*, vol. 178, no. 5, pp. 1053–1057, 2002.
- [20] C. C. Jaffe, "Measures of response: RECIST, WHO, and new alternatives," *J Clin Oncol*, vol. 24, pp. 3245–3251, 2006.
- [21] H. Jang, K. Lee, O. Kwon, and J. Rhee, YS. Han, "Bronchioloalveolar carcinoma: focal area of ground-glass attenuation at thin-section CT as an early sign," *Radiology*, vol. 199, p. 485488, 1996.

- [22] R. Kakinuma, H. Ohmatsu, M. Kaneko, M. Kusumoto, J. Yoshida, K. Nagai, and et al., “Progression of focal pure ground-glass opacity detected by low-dose helical computed tomography screening for lung cancer,” *J Comput Assist Tomogr*, vol. 28, p. 1723, 2004.
- [23] Y. Katsumata, Y. Itai, S. Maeda, H. Kim, J. Tan, and S. Ishikawa, “Automatic detection of GGO candidate regions employing four statistical features on thoracic MDCT images,” in *Int. Conf. Control, Automation and Systems*, (Seoul), 2007.
- [24] E. Kim, T. Johkoh, K. Lee, K. Fujimoto, J. Sadohara, P. Yang, T. Kozuka, O. Honda, and S. Kim, “Quantification of ground-glass opacity on high-resolution CT of small peripheral adenocarcinoma of the lung: pathologic and prognostic implications,” *AJR*, vol. 177, p. 14171422, 2001.
- [25] K. Kim, J. Goo, J. Kim, H. Lee, B. Min, K. Bae, and J. Im, “Computer-aided diagnosis of localized ground-glass opacity in the lung at CT: Initial experience,” *Radiology*, no. 237, pp. 657–661, 2005.
- [26] J. P. Ko and D. P. Naidich, “Lung nodule detection and characterization with multislice CT,” *Radiol. Clin. N. Am.*, vol. 41, pp. 575–597, 2003.
- [27] J. P. Ko and D. P. Naidich, “Computer-aided diagnosis and the evaluation of lung disease,” *J. Thorac Imaging*, vol. 19, pp. 136–155, 2004.
- [28] J. J. Koenderink, “The structure of images,” *Biol. Cybern.*, vol. 50, pp. 363–370, 1984.
- [29] W. J. Kostis, A. P. Reeves, D. F. Yankelevitz, and C. I. Henschke, “Three-dimensional segmentation and growth-rate estimation of small pulmonary nodules in helical CT images,” *IEEE Trans. Medical Imaging*, vol. 22, no. 10, pp. 1259–1274, 2003.
- [30] W. J. Kostis, D. F. Yankelevitz, A. P. Reeves, S. C. Fluture, and C. I. Henschke, “Small pulmonary nodules: reproducibility of three-dimensional volumetric measurement and estimation of time to follow-up CT,” *Radiology*, vol. 231, p. 446452, 2004.
- [31] T. Kubota, A. Jerebko, M. Salganicoff, M. Dewan, and A. Krishnan, “Robust segmentation of pulmonary nodules of various densities: from ground-glass opacities to solid nodules,” in *Int. Workshop. Pulmonary Image Processing*, (New York), 2008.
- [32] K. Kuriyama, M. Seto, T. Kasugai, S. Higashiyama, M. Kido, Y. Sawai, K. Kodama, and D. Kuroda, “Ground-glass opacity on thinsection CT: value in differentiating subtypes of adenocarcinoma of the lung,” *Am. J. Roentgenol*, vol. 173, p. 465469, 1999.

- [33] K. Lee, Y. Jeong, J. Han, B. Kim, H. Kim, and O. Kwon, "T1 non-small cell lung cancer: imaging and histopathologic findings and their prognostic implications," *Radiographics*, vol. 24, p. 16171636, 2004.
- [34] Y. Lee, T. Hara, H. Fujita, S. Itoh, and T. Ishigaki, "Automated detection of pulmonary nodules in helical CT images based on an improved template-matching technique," *IEEE Trans. Medical Imaging*, vol. 20, no. 7, pp. 595–604, 2001.
- [35] F. Li, S. Sone, H. Abe, H. MacMahon, and K. Doi, "Malignant versus benign nodules at CT screening for lung cancer: Comparison of thin-section CT findings," *Radiology*, vol. 233, pp. 793–798, 2004.
- [36] Q. Li, "Recent progress in computer-aided diagnosis of lung nodules on thin-section CT," *Comput Med Imaging Graph*, vol. 31, p. 248257, 2007.
- [37] Q. Li, F. Li, K. Suzuki, J. Shiraishi, H. Abe, R. Engelmann, Y. Nie, H. MacMahon, and K. Doi, "Computer-aided diagnosis in thoracic CT," *Semin Ultrasound CT MRI*, vol. 26, pp. 357–363, 2005.
- [38] T. Lindeberg, "Feature detection with automatic scale selection," *Int. J. Comput. Vision*, vol. 30, no. 2, pp. 79–116, 1998.
- [39] J. Min, H. Lee, K. Lee, J. Han, K. Park, M. Ahn, and S. Lee, "Stepwise evolution from a focal pure pulmonary ground-glass opacity nodule into an invasive lung adenocarcinoma: An observation for more than 10 years." In press, 2010.
- [40] R. Nakajima, T. Yokose, R. Kakinuma, K. Nagai, Y. Nishiwaki, and A. Ochiai, "Localized pure ground-glass opacity on high-resolution CT: histologic characteristics," *J Comput Assist Tomogr*, vol. 26, p. 323329, 2002.
- [41] M. Nakata, H. Saeki, I. Takata, Y. Segawa, H. Mogami, K. Mandai, and K. Eguchi, "Focal ground-glass opacity detected by low-dose helical CT," *Chest*, vol. 121, no. 5, pp. 1464–1467, 2002.
- [42] M. Noguchi, A. Morikawa, M. Kawasaki, and et al., "Small adenocarcinoma of the lung: histologic characteristics and prognosis," *Cancer*, vol. 75, p. 28442852, 1995.
- [43] B. Odry, J. Huo, L. Zhang, C. Novak, and D. Naidich, "Solid component evaluation in mixed ground glass nodules," in *SPIE*, volume 6512, 2007.
- [44] T. Ohtsuka, H. Nomori, H. Horio, T. Naruke, and K. Suemasu, "Radiological examination for peripheral lung cancers and benign nodules less than 10 mm," *Lung Cancer*, vol. 42, pp. 291–296, 2003.

- [45] K. Okada, D. Comaniciu, N. Dalal, and A. Krishnan, "A robust algorithm for characterizing anisotropic local structures," in *Euro. Conf. Computer Vision*, volume I, (Prague), 2004, pp. 549–561.
- [46] K. Okada, D. Comaniciu, and A. Krishnan, "Robust anisotropic gaussian fitting for volumetric characterization of pulmonary nodules in multislice CT," *IEEE Trans. Medical Imaging*, no. 24, pp. 409–423, 2005.
- [47] C. Park, J. Goo, H. Lee, C. Lee, E. Chun, and J. Im, "Nodular ground-glass opacity at thin-section CT: Histologic correlation and evaluation of change at follow-up," *RadioGraphics*, vol. 27, pp. 391–408, 2007.
- [48] A. P. Reeves, A. B. Chan, D. F. Yankelevitz, C. I. Henschke, B. Kressler, and W. J. Kostis, "On measuring the change in size of pulmonary nodules," *IEEE Trans. Med. Imaging*, vol. 25, pp. 435–450, 2006.
- [49] A. P. Reeves and W. J. Kostis, "Computer-aided diagnosis of small pulmonary nodules," *Seminars in Ultrasound, CT, and MRI*, vol. 21, no. 2, pp. 116–128, 2000.
- [50] A. P. Reeves and B. Kressler, "Computer-aided diagnostics," *Thorac Surg Clin*, vol. 14, pp. 125–133, 2004.
- [51] M. F. Rinaldi, T. Bartalena, L. Bracciaioli, N. Sverzellati, S. Mattioli, E. Rimondi, G. Rossi, M. Zompatori, G. Battista, and R. Canini, "Three-dimensional analysis of pulmonary nodules: variability of semiautomated volume measurements between different versions of the same software," *Radiol med*, vol. 115, pp. 403–412, 2010.
- [52] I. Sluimer, A. Schilham, M. Prokop, and B. van Ginneken, "Computer analysis of computed tomography scans of the lung: a survey," *IEEE Trans. Med. Imaging*, vol. 25, pp. 385–405, 2006.
- [53] M. Staring, J. P. W. Pluim, B. de Hoop, S. Klein, B. van Ginneken, H. Gietema, G. Nossent, C. Schaefer-Prokop, S. van de Vorst, and M. Prokop, "Image subtraction facilitates assessment of volume and density change in ground-glass opacities in chest CT," *Investigative Radiology*, vol. 44, pp. 61–66, 2009.
- [54] K. Suzuki, H. Asamura, K. Kusumoto, H. Kondo, and R. Tsuchiya, "Thin-section computed-tomographic scan," *Ann Thorac Surg*, vol. 74, pp. 1635–9, 2002.

- [55] K. Suzuki, F. Li, S. Sone, and K. Doi, "Computer-aided diagnostic scheme for distinction between benign and malignant nodules in thoracic low-dose CT by use of massive training artificial neural network," *IEEE Trans. Medical Imaging*, no. 24, pp. 1138–1150, 2005.
- [56] S. Takashima, Y. Maruyama, M. Hasegawa, T. Yamanda, T. Honda, M. Kadoya, and et al., "CT findings and progression of small peripheral lung neoplasms having a replacement growth pattern," *AJR Am J Roentgenol*, vol. 180, p. 81726, 2003.
- [57] M. Tanino, H. Takizawa, S. Yamamoto, T. Matsumoto, Y. Tateno, and T. Iimura, "A detection method of ground glass opacities in chest x-ray CT images using automatic clustering techniques," in *SPIE*, volume 5032, 2003, pp. 1728–1737.
- [58] Y. Tao, L. Lu, M. Dewan, A. Chen, J. Corso, J. Xuan, M. Salganicoff, and A. Krishnan, "Multi-level ground glass nodule detection and segmentation in CT lung images," in *Medical Image Computing and Computer-Assisted Intervention*, (London), 2009.
- [59] W. Travis, K. Garg, W. Franklin, and et al., "Evolving concepts in the pathology and computed tomography imaging of lung adenocarcinoma and bronchioloalveolar carcinoma," *J Clin Oncol*, vol. 23, pp. 3270–3287, 2005.
- [60] S. Watanabe, T. Watanabe, K. Arai, T. Kasai, J. Haratake, and H. Urayama, "Results of wedge resection for focal bronchioloalveolar carcinoma showing pure ground-glass attenuation on computed tomography," *Ann. Thorac. Surg.*, vol. 73, pp. 1071–1075, 2002.
- [61] H. K. Weir et al., "Annual report to the nation on the status of cancer, 1975-2000," *Journal of the National Cancer Institute*, vol. 95, no. 17, pp. 1276–1299, 2003.
- [62] A. Witkin, "Scale-space filtering," in *Int. Joint. Conf. Artificial Intell.*, (Karlsruhe), 1983, pp. 1019–1021.
- [63] Z. Yang, S. Sone, T. Takashima, and et al., "High-resolution CT analysis of small peripheral lung adenocarcinomas revealed on screening helical CT," *AJR Am J Roentgenol*, vol. 176, p. 13991407, 2001.
- [64] D. F. Yankelevitz, A. P. Reeves, W. J. Kostis, B. Zhao, and C. I. Henschke, "Small pulmonary nodules: volumetrically determined growth rates based on CT evaluation," *Radiology*, vol. 217, pp. 251–256, 2000.

- [65] X. Ye, X. Lin, J. Dehmeshki, G. Slabaugh, and G. Beddoe, "Shape based computer-aided detection of lung nodules in thoracic CT images," *IEEE Trans. Biomed. Eng.*, vol. 56, pp. 1810–20, 2009.
- [66] Y. Yoo, H. Shim, I. Yun, K. Lee, and S. Lee, "Segmentation of ground glass opacities by asymmetric multi-phase deformable model," in *SPIE*, volume 6144, 2006.
- [67] L. Zhang, M. Fang, D. Naidich, and C. Novak, "Consistent interactive segmentation of pulmonary ground glass nodules identified in CT studies," in *SPIE*, volume 5370, 2004, pp. 1709–1719.
- [68] L. Zhang, C. Zhang, T. Novak, D. Naidich, and D. Moses, "A computer-based method of segmenting ground glass nodules in pulmonary CT images: comparison to expert radiologists' interpretations," in *SPIE*, volume 5747, 2005, pp. 113–123.
- [69] Y. Zheng, C. Kambhamettu, T. Bauer, and K. Steiner, "Estimation of ground-glass opacity measurement in ct lung images," in *Medical Image Computing and Computer-Assisted Intervention*, (New York), 2008.
- [70] J. Zhou, S. Chang, D. N. Metaxas, B. Zhao, M. Ginsberg, and L. Schwartz, "An automatic method for ground-glass opacity nodule detection and segmentation from CT studies," in *Int. Conf. EMBS*, (New York), 2006.